

Article

Ceria Nanoparticles' Morphological Effects on the N₂O Decomposition Performance of Co₃O₄/CeO₂ Mixed Oxides

Maria Lykaki ¹, Eleni Papista ², Nikolaos Kaklidis ², Sónia A. C. Carabineiro ³ and Michalis Konsolakis ^{1,*}

¹ School of Production Engineering and Management, Technical University of Crete, 73100 Chania, Greece; mlykaki@isc.tuc.gr

² Department of Mechanical Engineering, University of Western Macedonia, GR-50100 Kozani, Greece; epapista@uowm.gr (E.P.); nkaklidis@uowm.gr (N.K.)

³ Laboratório de Catálise e Materiais (LCM), Laboratório Associado LSRE-LCM, Faculdade de Engenharia, Universidade do Porto, 4200-465 Porto, Portugal; scarabin@fe.up.pt

* Correspondence: mkonsol@pem.tuc.gr; Tel.: +30-28210-37682

Received: 15 January 2019; Accepted: 18 February 2019; Published: 3 March 2019



Abstract: Ceria-based oxides have been widely explored recently in the direct decomposition of N₂O (deN₂O) due to their unique redox/surface properties and lower cost as compared to noble metal-based catalysts. Cobalt oxide dispersed on ceria is among the most active mixed oxides with its efficiency strongly affected by counterpart features, such as particle size and morphology. In this work, the morphological effect of ceria nanostructures (nanorods (NR), nanocubes (NC), nanopolyhedra (NP)) on the solid-state properties and the deN₂O performance of the Co₃O₄/CeO₂ binary system is investigated. Several characterization methods involving N₂ adsorption at −196 °C, X-ray diffraction (XRD), temperature programmed reduction (TPR), X-ray photoelectron spectroscopy (XPS) and transmission electron microscopy (TEM) were carried out to disclose structure–property relationships. The results revealed the importance of support morphology on the physicochemical properties and the N₂O conversion performance of bare ceria samples, following the order nanorods (NR) > nanopolyhedra (NP) > nanocubes (NC). More importantly, Co₃O₄ impregnation to different carriers towards the formation of Co₃O₄/CeO₂ mixed oxides greatly enhanced the deN₂O performance as compared to bare ceria samples, without, however, affecting the conversion sequence, implying the pivotal role of ceria support. The Co₃O₄/CeO₂ sample with the rod-like morphology exhibited the best deN₂O performance (100% N₂O conversion at 500 °C) due to its abundance in Co²⁺ active sites and Ce³⁺ species in conjunction to its improved reducibility, oxygen kinetics and surface area.

Keywords: ceria nanoparticles; morphological effects; Co₃O₄/CeO₂ mixed oxides, deN₂O process

1. Introduction

Nitrous oxide (N₂O) is one of the most significant greenhouse gases contributing to the depletion of the ozone layer. N₂O has a much higher global warming potential (GWP) compared to CO₂ (310 times higher) and a long atmospheric lifetime (114 years). The emissions of N₂O are derived by both natural and anthropogenic sources. The main anthropogenic sources for N₂O emissions involve agriculture (use of fertilizers), chemical industry (adipic and nitric acid production), the combustion of fossil fuels, as well as biomass burning, etc. [1–4].

The abatement of N₂O emissions is of paramount importance and the direct catalytic decomposition of nitrous oxide to molecular nitrogen and oxygen (deN₂O process) is considered to be a highly efficient remediation method. Thus far, several catalytic systems, such as supported noble

metals [5–7], perovskites [8–10], hexaaluminates [11–14], spinels [15–18], zeolites [19–22] and mixed oxides [23–27], have been used for N₂O decomposition. Although noble metals exhibit satisfactory activity for the deN₂O process, their high cost and the deterioration of their catalytic efficiency from gases present in the exhaust gas stream (e.g., O₂) act as inhibiting factors for practical applications [1,28]. Hence, research efforts have focused on the development of noble metal-free mixed oxides of high activity, stability and low cost, as recently reviewed [1].

Among the different transition metal oxides, cobalt spinel shows unique physicochemical characteristics, such as thermal stability and high reducibility, making it an excellent candidate for the deN₂O process [15,23,29,30]. However, the high cost of cobalt renders mandatory its dispersion to high surface area supports like ceria, magnesia, etc. [31,32]. Among the various supports investigated, ceria exhibits unique redox properties associated with its high oxygen storage capacity (OSC), rendering this material highly effective in many catalytic processes [23,33–35]. Furthermore, the synergistic effects induced by strong metal–ceria interactions, in nanoscale, can modify the surface chemistry of the materials through geometric or/and electronic perturbations, leading to improved redox properties and catalytic activity [36–40].

However, the catalytic efficiency of transition metal oxides, involving ceria-based mixed oxides, can be considerably affected by the different counterpart characteristics, such as particle size and morphology. In this regard, engineering the particle size and shape (e.g., nanorods and nanocubes) through the employment of advanced nano-synthesis paths has lately received particular attention [33,41–43]. Interestingly, the support morphology greatly affects the redox properties, oxygen mobility and, subsequently, the catalytic activity of the mixed oxides. For instance, Lin et al. [44] prepared Co₃O₄/CeO₂ catalysts with three different support morphologies, namely polyhedra, nanorods and hexagonal shapes, with polyhedra exhibiting the highest catalytic activity for ammonia synthesis. In a similar manner, by tailoring the support morphology, CuO/CeO₂ nanoshaped materials of enhanced reducibility and deN₂O performance can be obtained [45]. Andrade-Martínez et al. [46] investigated the catalytic reduction of N₂O over CuO/SiO₂ catalysts, revealing the key role of the spherical ordered mesoporous support, along with its functionalization through copper addition, on the improved catalytic activity and stability, making this material comparable to noble metal-reported systems. Different support morphologies (rods, plates and cubes) have also been employed for the low temperature CH₂Br₂ oxidation revealing the superiority of cobalt-ceria nanorods in the catalytic performance [47]. Moreover, cobalt oxide supported on ceria of different morphology (nanoparticles, nanorods and nanocubes) has been investigated for the catalytic oxidation of toluene with the nanoparticles exhibiting the highest catalytic activity due to the synergism at the interface between the two oxide phases, which leads to an improved reducibility [48]. Very recently, the influence of support morphology (nanorods, nanocubes and nanopolyhedra) on the surface and structural properties of CuO/CeO₂ mixed oxide has been thoroughly explored through both *in situ* and *ex situ* characterization techniques. The results disclosed the significance of the ceria morphology on the reducibility and oxygen kinetics, revealing the order nanorods > nanopolyhedra > nanocubes [49].

In this work, ceria structures of various morphologies (nanopolyhedra, nanorods and nanocubes) were hydrothermally prepared, and then cobalt was impregnated into the above ceria supports. The purpose of this work was to explore the impact of support morphology on the surface chemistry and the deN₂O performance of Co₃O₄/CeO₂ mixed oxides. The results clearly revealed that support morphology can exert a profound influence on the N₂O decomposition, paving the way toward the rational design of highly efficient deN₂O catalysts.

2. Results and Discussion

2.1. Textural/Structural Analysis (BET and XRD)

The main textural and structural characteristics of bare ceria samples and Co₃O₄/CeO₂ mixed oxides (hereinafter denoted as Co/CeO₂) are summarized in Table 1. According to the BET surface area,

the following order is acquired: CeO₂-NP (88 m² g⁻¹) > CeO₂-NR (79 m² g⁻¹) > CeO₂-NC (37 m² g⁻¹). The addition of cobalt into CeO₂ decreases the surface area, without, however, significantly affecting the order obtained for bare ceria samples. The Co/CeO₂-NR sample exhibits the highest value (72 m² g⁻¹) succeeded by Co/CeO₂-NP (71 m² g⁻¹) and Co/CeO₂-NC (28 m² g⁻¹). Regarding the average pore diameter and pore volume, they both decreased upon the addition of Co to ceria nanorods and nanocubes. However, concerning ceria nanopolyhedra, the addition of cobalt leads to a small increase in the average pore diameter, whereas the pore volume is not significantly affected (Table 1).

Table 1. The textural and structural properties of bare CeO₂ and Co/CeO₂ samples.

Sample	BET Analysis			XRD Analysis	
	BET Surface Area (m ² g ⁻¹)	Pore Volume (cm ³ /g)	Average Pore Diameter (nm)	Crystallite Size (nm), D _{XRD} ¹	
				CeO ₂	Co ₃ O ₄
CeO ₂ -NC	37	0.26	27.4	27 ± 1	-
CeO ₂ -NR	79	0.48	24.2	15 ± 1	-
CeO ₂ -NP	88	0.17	7.9	11 ± 1	-
Co/CeO ₂ -NC	28	0.15	22.6	24 ± 1	19 ± 1
Co/CeO ₂ -NR	72	0.31	17.4	14 ± 1	16 ± 1
Co/CeO ₂ -NP	71	0.17	9.8	11 ± 1	15 ± 1

¹ Calculated applying the Williamson–Hall plot after the Rietveld refinement of diffractograms.

Figure 1a shows the Barret-Joyner-Halenda (BJH) desorption pore size distributions (PSD) of bare ceria and Co/CeO₂ catalysts. According to the pore size distribution, all the samples have their maxima at a pore diameter more than 3 nm, designating the presence of mesopores [50]. It is obvious that bare ceria samples with the nanocube (CeO₂-NC) and nanorod morphology (CeO₂-NR) exhibit similar particle size distributions, whereas in ceria nanopolyhedra (CeO₂-NP), a narrower PSD is observed. Noteworthy, PSD remains practically unaffected by the addition of cobalt in all cases. As it can be observed in Figure 1b which shows the adsorption–desorption isotherms, all samples demonstrate type IV isotherms with a hysteresis loop at a relative pressure > 0.5, further corroborating the mesoporous structure of the materials [51,52].

The XRD patterns of the samples are shown in Figure 2. The main peaks can be indexed to (111), (200), (220), (311), (222), (400), (331), (420), (422), (511) and (440) planes which are attributed to ceria face-centered cubic fluorite structure (Fm3m symmetry, no. 225) [53,54]. There are three small peaks at 2θ values of approx. 36, 44 and 64° which are typical of Co₃O₄ [33]. These three diffraction peaks correspond to the (311), (400) and (440) planes of Co₃O₄, respectively. The average crystallite diameter of the oxide phases (CeO₂ and Co₃O₄) was assessed by an XRD analysis by means of the Williamson–Hall plot (Table 1). The CeO₂ crystallite size measurements showed 24, 14 and 11 nm for Co/CeO₂-NC, Co/CeO₂-NR and Co/CeO₂-NP, respectively. As it is obvious from Table 1, there is a small decrease in the ceria crystallite size for nanocubes and nanorods, whereas no changes were observed for nanopolyhedra, indicating that the structural characteristics of ceria supports do not get significantly affected upon cobalt addition, as it will be further corroborated by a TEM analysis (see below). In a similar manner, the BET analysis (Table 1) indicates no significant modifications on the pore characteristics of ceria nanopolyhedra upon cobalt addition, which could be ascribed to their irregular morphology. It should be also noted that the samples with nanocube morphology exhibit the smallest BET surface area and the largest CeO₂ and Co₃O₄ crystallite sizes in comparison to nanorods and nanopolyhedra. As for the crystallite size of cobalt oxide phase, the following sequence was obtained: Co/CeO₂-NC (19 nm) > Co/CeO₂-NR (16 nm) > Co/CeO₂-NP (15 nm), which perfectly matches the order obtained for CeO₂.

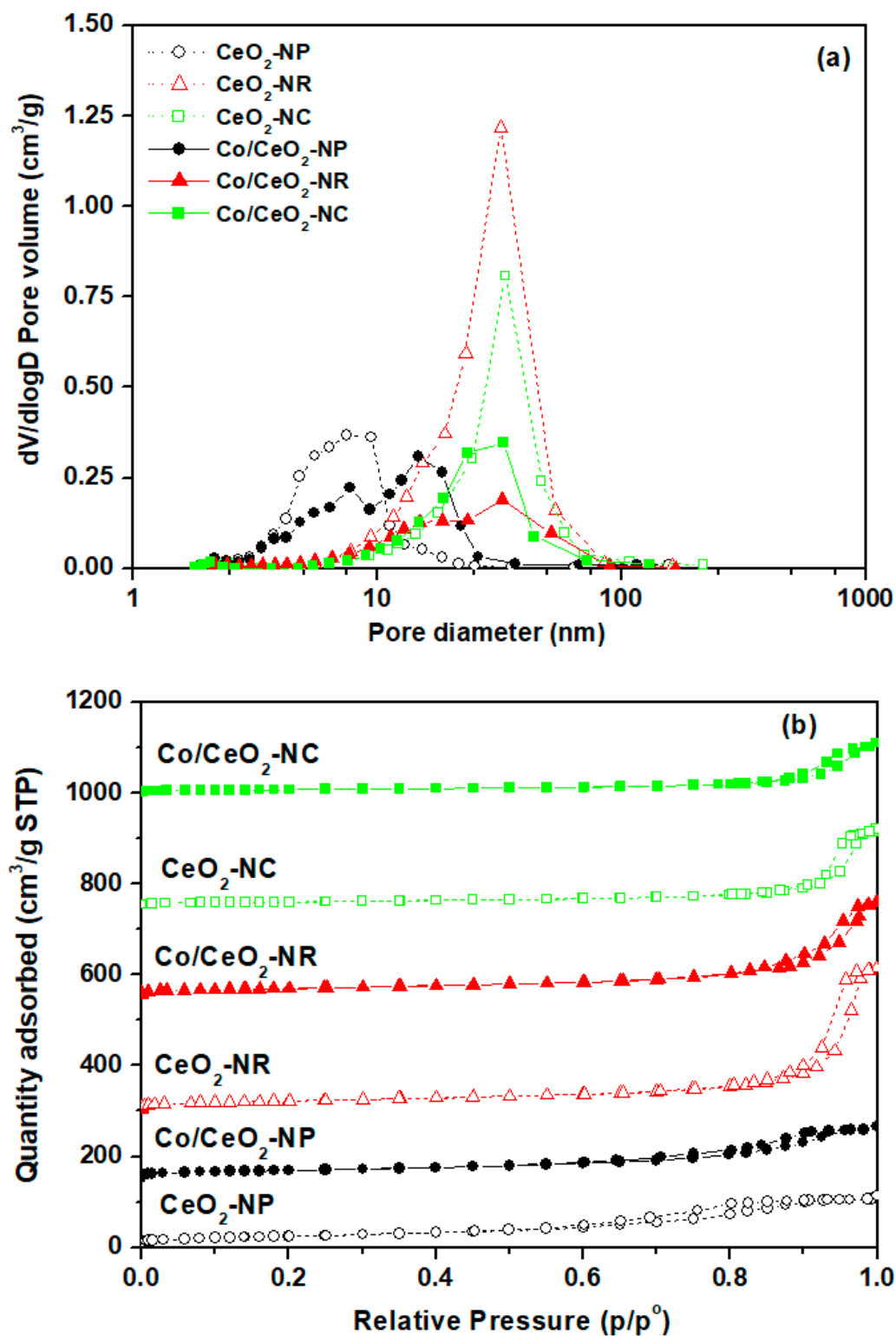


Figure 1. (a) The BJH (Barret-Joyner-Halenda) desorption pore size distribution (PSD) and (b) the adsorption–desorption isotherms of CeO_2 and Co/CeO_2 samples.

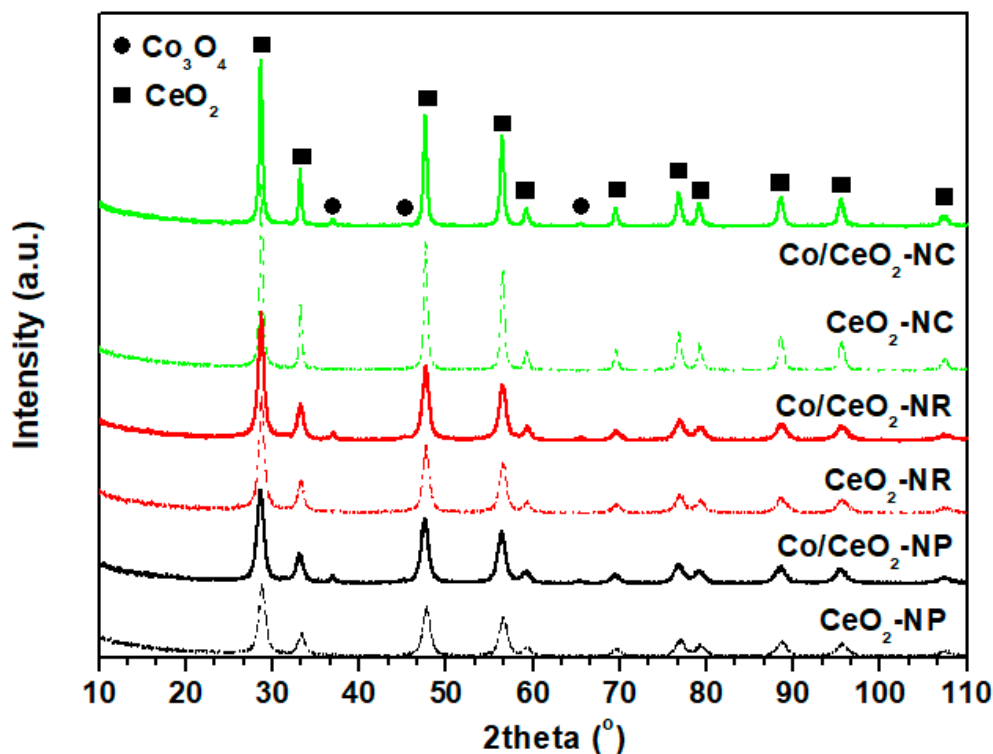


Figure 2. The XRD patterns of the CeO₂ and Co/CeO₂ samples.

2.2. Morphological Characterization (TEM)

Transmission electron microscopy (TEM) has been applied so as to examine the morphological differences among the materials. Figure 3a–c shows the TEM images of ceria supports. The CeO₂-NR sample (Figure 3a) exhibits a rod-shaped morphology with the length varying between 25 and 200 nm. Figure 3b and c demonstrates mainly irregular-shaped nanopolyhedra and cubes, respectively. Figure 3d–f illustrates the images derived by TEM analysis for the Co/CeO₂ mixed oxides. Evidently, the morphology is not affected by cobalt addition to the ceria carrier.

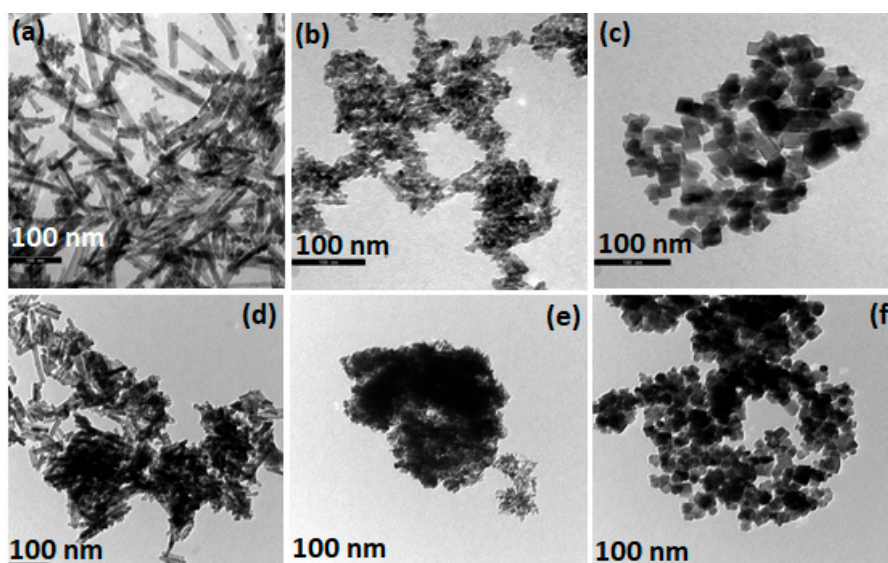


Figure 3. The transmission electron microscopy images of CeO₂ (a–c) and Co/CeO₂ (d–f) samples: (a) CeO₂-NR, (b) CeO₂-NP, (c) CeO₂-NC, (d) Co/CeO₂-NR, (e) Co/CeO₂-NP and (f) Co/CeO₂-NC.

2.3. Redox Properties (H_2 -Temperature Programmed Reduction (TPR))

H_2 -TPR experiments took place to investigate the ceria shape effect on the redox properties of as-prepared samples. Figure 4a shows the TPR profiles of bare ceria samples, consisting of two wide-ranging peaks which are centred at 526–551 °C and 789–813 °C. These peaks are attributed to ceria surface oxygen (O_s) and bulk oxygen (O_b) reduction, respectively [33,49,55]. In Table 2, the hydrogen consumption corresponding to surface oxygen as well as to bulk oxygen reduction is presented. Based on the ratio of surface-to-bulk oxygen (O_s/O_b), the following order was acquired: CeO_2 -NR (1.13) > CeO_2 -NP (0.94) > CeO_2 -NC (0.71). This indicates the superior reducibility of the rod-shaped sample as it exhibits the highest amount of loosely bound oxygen species. The latter is expected to notably affect the de N_2O process, where the desorption of adsorbed oxygen species mainly determines the reaction rate (*vide infra*).

Table 2. The redox properties of the bare CeO_2 and Co/ CeO_2 samples.

Sample	H_2 Consumption ($mmol H_2 g^{-1}$) ^a			O_s/O_b Ratio	Peak Temperature (°C)	
	O_s Peak	O_b Peak	Total		O_s Peak	O_b Peak
CeO_2 -NP	0.48	0.51	0.99	0.94	555	804
CeO_2 -NR	0.59	0.52	1.11	1.13	545	788
CeO_2 -NC	0.41	0.58	0.99	0.71	589	809
	Peaks a+b	CeO_2 Peak	Total		Peak a	Peak b
Co/ CeO_2 -NP	2.40	0.61	3.01		333	388
Co/ CeO_2 -NR	2.37	0.62	2.99		318	388
Co/ CeO_2 -NC	2.05	0.32	2.37		335	405

^a Estimated by the area of the corresponding temperature programmed reduction (TPR) peaks, which is calibrated against a known amount of CuO standard sample.

The reduction profiles of the Co/ CeO_2 samples as well as the one of a Co_3O_4 reference are shown in Figure 4b. Table 2 summarizes the main TPR peaks along with the hydrogen consumption ($mmol H_2 g^{-1}$). Pure Co_3O_4 shows two reduction peaks (a and b) in much lower temperatures than those of bare ceria samples, namely 305 °C and 415 °C. They are ascribed to the stepwise reduction of $Co_3O_4 \rightarrow CoO \rightarrow Co$, respectively [44,56–58].

On the other hand, Co/ CeO_2 samples exhibit two main peaks at the temperature range of 318–335 °C (peak a) and 388–405 °C (peak b), ascribed to the reduction of Co^{3+} to Co^{2+} and Co^{2+} to Co^0 , respectively [33,59,60]. Obviously, the cobalt addition facilitates the reduction of ceria surface oxygen, shifting the peaks centered at 526–551 °C to a lower temperature (comparison of Figure 4a,b). They also exhibit a broad peak above 800 °C, attributed to the ceria subsurface oxygen reduction, while the capping oxygen reduction overlaps with the reduction of CoO [33,56,61]. Apparently, the reduction of the mixed oxides takes place in lower temperatures compared to the bare ceria samples, demonstrating the beneficial effect of cobalt on the surface oxygen reduction of ceria. In fact, the interaction between the two oxide phases could be considered responsible for the improved reducibility and oxygen mobility, as thoroughly discussed in previous studies [48,49,62]. According to the consumption of hydrogen in the low-temperature range (Table 2), which could be related to the cobalt species reduction along with the ceria surface oxygen reduction, the Co/ CeO_2 -NP and Co/ CeO_2 -NR samples exhibit a similar H_2 uptake (about 2.40 $mmol H_2 g^{-1}$) while the sample of nanocube morphology exhibits a much lower value (2.05 $mmol H_2 g^{-1}$). This trend is well-matched to the catalytic results (*vide infra*), revealing the key role of redox ability on the de N_2O process.

Moreover, the Co/ CeO_2 -NR sample exhibits the lowest reduction temperature (peak at 318 °C) in comparison with the other samples (peak ca. 335 °C), indicating the facilitation of Co^{3+} species reduction over ceria nanorods. Noteworthily, the theoretical amount of hydrogen for the complete reduction of Co_3O_4 to Co (approx. 1.76 $mmol H_2 g^{-1}$, based on a 7.8 wt. % nominal loading of Co) is always surpassed by the hydrogen amount required for the reduction of Co/ CeO_2 samples (Table 2).

The latter reveals the facilitation of ceria capping oxygen reduction in the presence of cobalt, further corroborating the above findings.

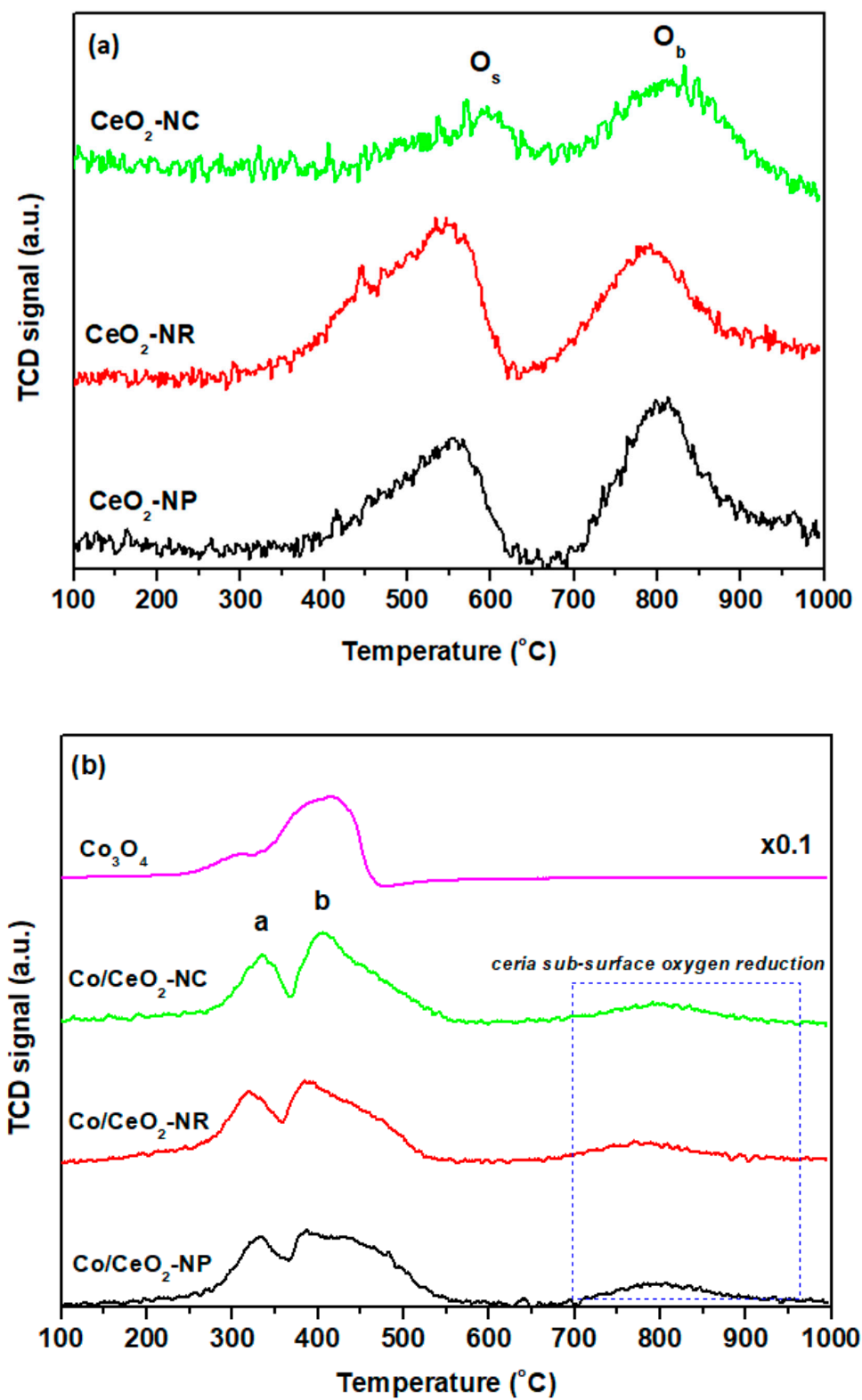


Figure 4. The H₂-TPR profiles of (a) bare CeO₂ and (b) Co₃O₄, Co/CeO₂ samples.

2.4. Surface Analysis (X-ray Photoelectron Spectroscopy (XPS))

An XPS analysis was performed in order to investigate the effect of ceria morphology on the elemental chemical states and surface composition of Co/CeO₂ mixed oxides. Figure 5a shows the Ce3d XPS spectra of ceria nanoparticles of different morphology and the corresponding Co/CeO₂ samples, which can be deconvoluted into eight components [63–65], with the assignment of the characteristic peaks having been thoroughly described in our previous work [49]. In brief, the three pairs of peaks labeled as u, v; u'', v''; and u''', v''' are ascribed to Ce⁴⁺, whereas the residual u' and v' peaks are ascribed to Ce³⁺ species.

The corresponding O 1s spectra of the samples are depicted in Figure 5b. The low binding energy peak at 529.3 eV is attributed to the lattice oxygen (O_I) of Co₃O₄ and CeO₂ phases, and the high binding energy peak at 531.3 eV corresponds to the chemisorbed oxygen (O_{II}) such as adsorbed oxygen (O⁻/O₂²⁻) and water, carbonate as well as hydroxyl species [23,56].

The proportion of Ce³⁺ (%) as well as the O_{II}/O_I ratio for all samples is summarized in Table 3. Bare ceria supports exhibit a similar amount of Ce³⁺ ranging from 23.3 to 25.3%. Regarding, the cobalt-ceria samples, the population of Ce³⁺ species is slightly higher, varying between 26.1 and 28.5%. In particular, the Co/CeO₂-NR sample exhibits the highest amount (28.5%) followed by Co/CeO₂-NP (26.7%) and Co/CeO₂-NC (26.1%), indicating the abundance of the nanorod samples in oxygen vacancies. Interestingly, the relative ratio of adsorbed to lattice oxygen (O_{II}/O_I) and the Ce³⁺ (%) follow the same order, namely, Co/CeO₂-NR (0.60) > Co/CeO₂-NP (0.53) > Co/CeO₂-NC (0.51), perfectly matched to the order obtained for the catalytic performance, as it will be discussed in the sequence. It should be also noted that Co addition to CeO₂-NR enhances both the population of reduced Ce³⁺ species and the O_{II}/O_I ratio, revealing the synergistic interactions between cerium and cobalt oxides toward the formation of highly reducible composites, in agreement with the TPR results.

Table 3. The XPS results of bare CeO₂ and Co/CeO₂ samples.

Sample	Co ²⁺ /Co ³⁺	Ce ³⁺ (%)	O _{II} /O _I
CeO ₂ -NC	-	23.3	0.50
CeO ₂ -NR	-	24.3	0.47
CeO ₂ -NP	-	25.3	0.49
Co/CeO ₂ -NC	1.06	26.1	0.51
Co/CeO ₂ -NR	1.32	28.5	0.60
Co/CeO ₂ -NP	0.94	26.7	0.53

Figure 6 depicts the Co 2p XPS spectra of Co/CeO₂ samples along with the spectrum obtained for the Co₃O₄ reference sample for comparison purposes. The samples exhibit two major peaks of Co2p_{3/2} (780 eV) and Co2p_{1/2} (795 eV). According to peaks' positions and shapes, the structure of the cobalt spinel is formed [23,66,67]. The Co²⁺/Co³⁺ ratio of Co/CeO₂ samples derived by the deconvolution of the Co2p_{1/2} and Co2p_{3/2} peaks is included in Table 3. The nanorod sample, which offers the best deN₂O performance (*vide infra*), exhibits the highest Co²⁺/Co³⁺ ratio (1.32), followed by nanocubes (1.06) and nanopolyhedra (0.94). In view of this fact, it has been reported that samples with a high Co²⁺/Co³⁺ ratio exhibit better deN₂O performance [3,20,22,43,59], further corroborating the present findings.

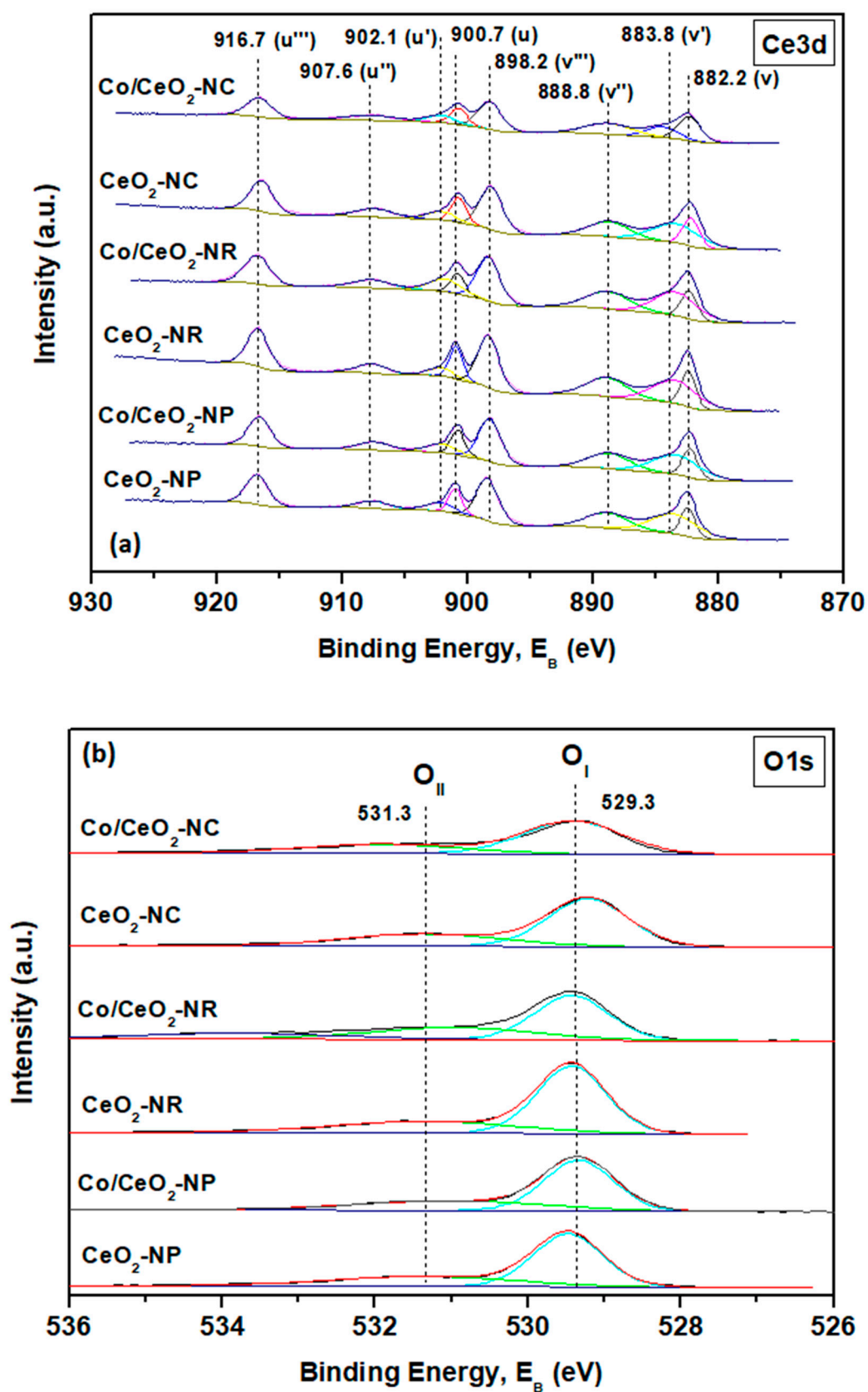


Figure 5. The X-ray photoelectron spectroscopy (XPS) spectra of (a) Ce 3d and (b) O 1s of bare CeO₂ and Co/CeO₂ samples.

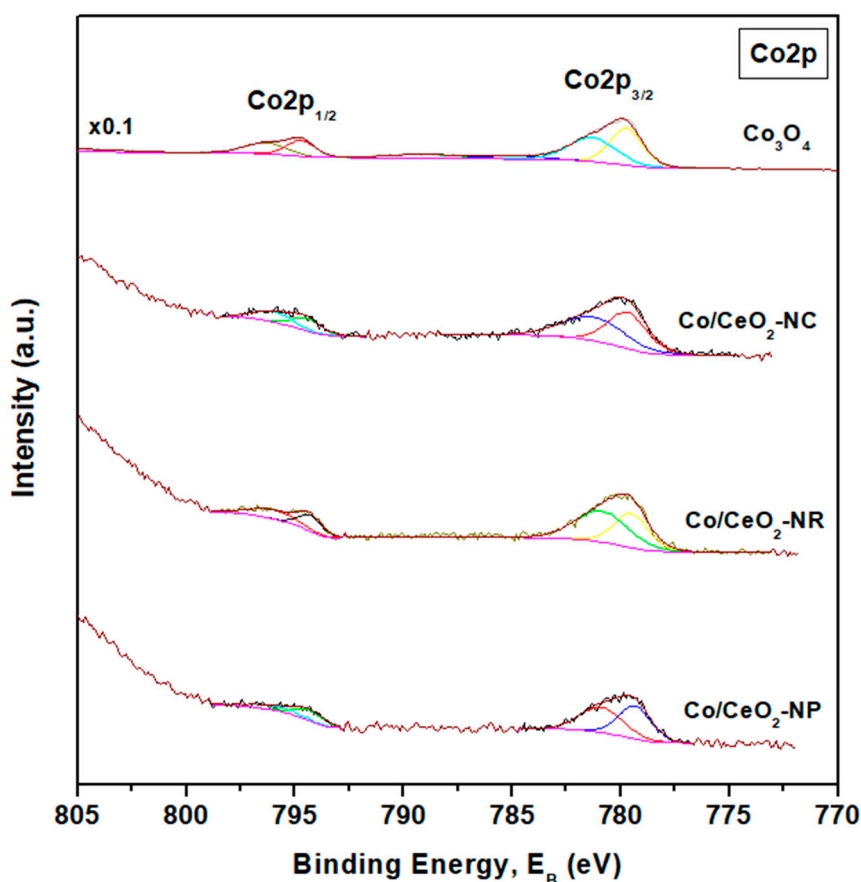


Figure 6. The Co 2p XPS spectra of the Co_3O_4 and Co/CeO_2 samples: The Co 2p XPS spectra of Co/CeO_2 samples have been magnified.

2.5. Catalytic Evaluation Studies

The impact of ceria morphology on the catalytic decomposition of N_2O under oxygen deficient and oxygen excess conditions was next examined. Figure 7a,b shows the N_2O conversion profiles as a temperature function for bare ceria as well as Co/CeO_2 samples in the absence and presence of oxygen, respectively. The $\text{Co}/\text{CeO}_2\text{-NR}$ sample exhibits the best catalytic performance, both in the absence and presence of oxygen in the gas stream. Apparently, the addition of cobalt in the ceria lattice enormously enhances the catalytic efficiency without, however, affecting the catalytic order of bare ceria samples, suggesting the pivotal role of ceria morphology on the deN_2O performance. In terms of the half-conversion temperature (T_{50}), the following order is obtained for the mixed oxides in the absence of oxygen: $\text{Co}/\text{CeO}_2\text{-NR}$ (449 °C) > $\text{Co}/\text{CeO}_2\text{-NP}$ (458 °C) > $\text{Co}/\text{CeO}_2\text{-NC}$ (464 °C). The same trend is observed in the presence of oxygen as well, although in slightly higher temperatures, due to its competitive sorption on the catalyst surface. In this point, it should be noted that the un-catalyzed reaction shows nearly zero N_2O conversion in the temperature range investigated, as previously reported [29,46,68].

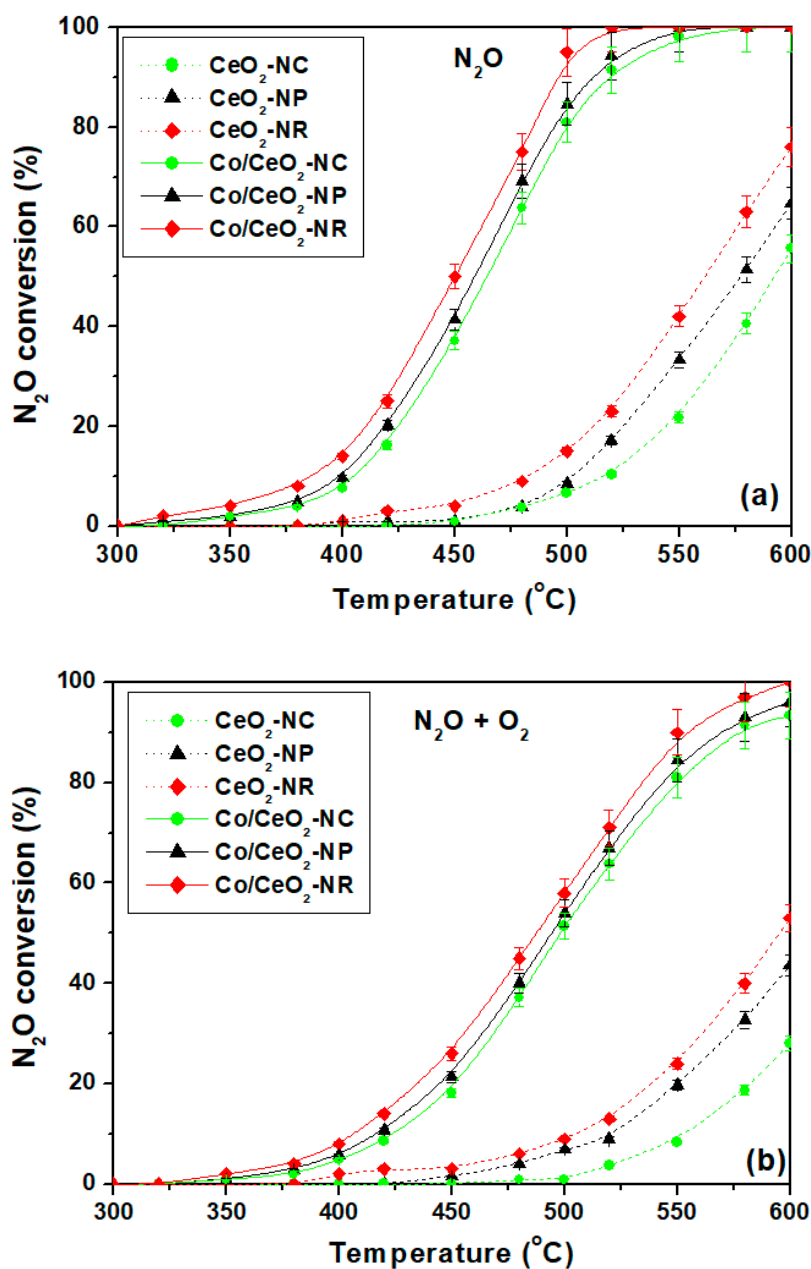


Figure 7. N_2O conversion as a function of temperature for CeO_2 and Co/CeO_2 samples of different morphology (a) in the absence and (b) in the presence of oxygen: The reaction conditions are 1000 ppm N_2O , 0 or 2% O_2 and Gas Hour Space Velocity (GHSV) = 40,000 h^{-1} .

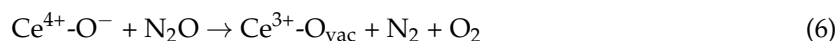
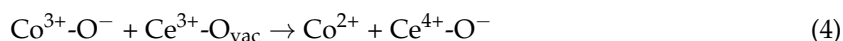
The above findings can be well-interpreted by taking into account a redox-type mechanism for the decomposition of N_2O over cobalt spinel oxides [4,23,24,30,59,69–73]:



In this mechanistic sequence, N_2O is initially chemisorbed on the Co^{2+} sites (Equation (1)) which are considered as the active centres for initiating the N_2O dissociative adsorption. Then, the regeneration of the active sites is taking place through the Co^{3+}/Co^{2+} redox cycle, involving the

combination of O^- into O_2^- (Equation (2)) and the desorption of molecular oxygen (Equation (3)), which finally leads to the regeneration of those sites [69].

However, in the case of Co_3O_4/CeO_2 mixed oxides, the excellent redox characteristics of ceria, such as oxygen storage capacity and oxygen mobility, can be further accounted for the regeneration of active sites through the following steps [69]:



Based on the above mechanistic scheme, the superiority of the Co/CeO_2 sample with a rod-like morphology can receive a consistent explanation. More specifically, nanorod-shaped ceria with (110) and (100) reactive planes exhibit enhanced oxygen kinetics and reducibility as it has the highest population of loosely bound oxygen species (Table 2), which is a decisive factor in terms of deN_2O activity. In other words, the high amount of weakly bound oxygen species present in the Co_3O_4/CeO_2 samples of rod-like morphology, linked directly to oxygen vacancy formation and oxygen mobility, could be considered responsible for the formation and the consequent regeneration of active sites. In this regard, a perfect interrelation between the catalytic performance (in terms of the half-conversion temperature, T_{50}) and the redox properties (in terms of the ratio of surface oxygen to bulk oxygen, O_s/O_b) is disclosed, as illustrated in Figure 8. This clearly justifies the key role of redox properties on the deN_2O process. In a similar manner, Liu et al. [28] have pointed out that the synergistic interaction between the two oxide phases in a $CuO-CeO_2$ mixed oxide enhances the reducibility and consequently the deN_2O efficiency as the surface-adsorbed oxygen species is easily desorbed and the active sites' regeneration is enabled.

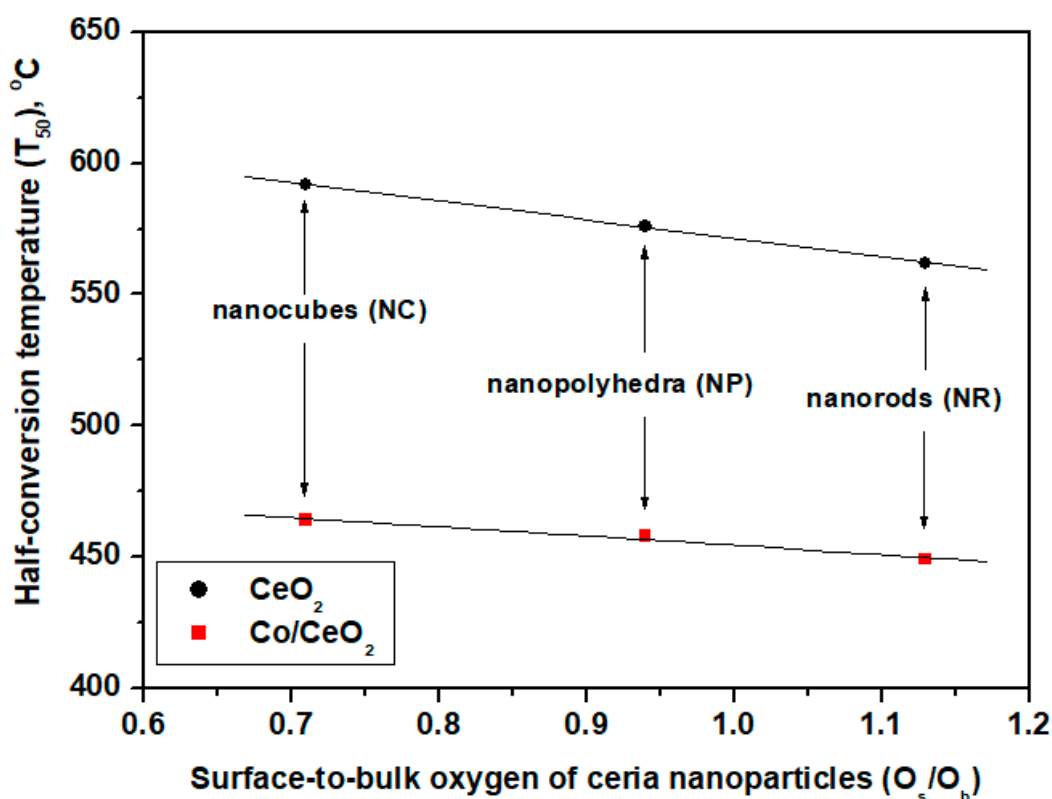


Figure 8. The half-conversion temperature (T_{50}) as a function of the TPR surface-to-bulk oxygen ratio (O_s/O_b).

More interestingly, the deN₂O performance of CeO₂ as well as the Co₃O₄/CeO₂ samples totally coincides, indicating the significance of the ceria carrier. However, the superiority of the mixed oxides in comparison to the bare ceria samples is evident, reflecting the synergistic interactions between cobalt and cerium oxides. The latter is manifested by the improved redox properties (in terms of H₂ consumption and TPR onset temperature) of Co₃O₄/CeO₂ mixed oxides as compared to bare ceria (Table 2). In a similar manner, the incorporation of cobalt into the ceria lattice increases both the amount of the adsorbed oxygen species (O⁻/O₂²⁻) and Ce³⁺ (Table 3), related with the surface oxygen reduction and the abundance in oxygen vacancies (O_{vac}).

Moreover, ceria nanorods facilitate the reduction of Co³⁺ to Co²⁺ active sites (Table 3), further contributing to the superior catalytic performance of the Co/CeO₂-NR sample. Along the same line, it has been recently reported that ceria nanorods stabilize the partial oxidation state of Co in CoO_x/CeO₂ catalysts *via* the facilitation of oxygen transfer at the metal-support interface [74]. It should be, therefore, deduced that ceria nanorods with the exposed (110) and (100) facets show the highest surface-to-bulk oxygen ratio resulting in improved reducibility and oxygen kinetics while exhibiting the highest amount of weakly bound oxygen species which is a decisive factor in the deN₂O process. Upon cobalt addition, the nanorod sample exhibits in addition the highest population in Ce³⁺/Co²⁺ redox pairs, indicative of abundant oxygen vacancies, which, along with its enhanced reducibility, leads to a superior deN₂O performance.

In this point, the enhanced textural characteristics (BET area and pore volume) of Co/CeO₂-NR as compared to Co/CeO₂-NC should be also mentioned, which could be further accounted for its enhanced deN₂O performance. Thus, by taking into account the specific activity normalized per unit of surface area (nmol m⁻² s⁻¹) instead of mass unit (nmol g⁻¹ s⁻¹), an inferior performance is observed for Co/CeO₂-NR compared to Co/CeO₂-NC (Table 4). On the other hand, Co₃O₄/CeO₂-NR exhibits a superior deN₂O performance (both in terms of conversion and specific activity) as compared to Co₃O₄/CeO₂-NP despite their similar structural (crystallite size) and textural (surface area) properties (Table 1). The latter clearly reveals the importance of exposed facets and redox properties on the deN₂O process, as it has been similarly reported by Zabilskiy et al. [45] for CuO/CeO₂ nanostructures of different morphology. Therefore, on the basis of the present findings, it can be deduced that the enhanced N₂O conversion performance of Co₃O₄/CeO₂-NR mixed oxides could be attributed to a compromise between redox and textural characteristics.

Table 4. The N₂O conversion and specific activity of Co/CeO₂ samples at 420 °C: The reaction conditions are 1000 ppm N₂O, 0 or 2 vol. % O₂ and GHSV = 40,000 h⁻¹.

Sample	N ₂ O Conversion (%)		Specific Activity			
	O ₂ Absence	O ₂ Presence	O ₂ Absence		O ₂ Presence	
			r (nmol g ⁻¹ s ⁻¹)	r (nmol m ⁻² s ⁻¹)	r (nmol g ⁻¹ s ⁻¹)	r (nmol m ⁻² s ⁻¹)
Co/CeO ₂ -NC	16.2	8.6	166	5.9	88	3.1
Co/CeO ₂ -NP	20.2	10.7	207	2.9	109	1.5
Co/CeO ₂ -NR	25	14	256	3.6	143	2.0

3. Materials and Methods

3.1. Materials Synthesis

In the present work, the chemicals that were used were of analytical reagent grade. Ce(NO₃)₃·6H₂O (Fluka, Bucharest, Romania, purity ≥99.0%) and Co(NO₃)₂·6H₂O (Sigma-Aldrich, Taufkirchen, Germany, purity ≥98%) were employed as precursor compounds for the preparation of bare ceria as well as Co/CeO₂ mixed oxides. Also, NaOH (Sigma-Aldrich, Taufkirchen, Germany, purity ≥98%) and ethanol (ACROS Organics, Geel, Belgium, purity 99.8%) were used during materials synthesis. Initially, the hydrothermal method was applied for the preparation of bare ceria nanoparticles, as described in detail in our previous work [49]. In brief, ceria nanorods (CeO₂-NR) were synthesized by dissolving NaOH (36.7 M) in double deionized water and then adding an appropriate

amount of an aqueous solution of $\text{Ce}(\text{NO}_3)_3 \cdot 6\text{H}_2\text{O}$ (0.13 M) under vigorous stirring. Next, the transfer of the final slurry into a Teflon bottle and its aging at $90\text{ }^\circ\text{C}$ for 24 h occurred. For the synthesis of ceria nanopolyhedra ($\text{CeO}_2\text{-NP}$), a similar procedure was followed, employing, however, a lower amount of NaOH (6 M). In order to synthesize ceria nanocubes ($\text{CeO}_2\text{-NC}$), the same procedure as the one described above for the synthesis of ceria nanorods was followed, with the obtained slurry to be aged at $180\text{ }^\circ\text{C}$ instead of $90\text{ }^\circ\text{C}$. In all cases, centrifugation was used for the recovery of the solid products that were thoroughly washed with double deionized water until a neutral pH was reached and finally washed with ethanol so as to avoid the nanoparticles' agglomeration. Afterwards, drying of the precipitate at $90\text{ }^\circ\text{C}$ for 12 h followed by calcination at $500\text{ }^\circ\text{C}$ for 2 h under air flow (heating ramp $5\text{ }^\circ\text{C}/\text{min}$) was carried out.

The Co/ $\text{CeO}_2\text{-NX}$ catalysts where NX stands for NP: nanopolyhedra, NR: nanorods and NC: nanocubes were prepared by wet impregnation, employing an aqueous solution of $\text{Co}(\text{NO}_3)_2 \cdot 6\text{H}_2\text{O}$, in order to achieve an atomic ratio $\text{Co}/(\text{Co}+\text{Ce})$ of 0.2 which corresponds to 7.8 wt. % of Co loading. Heating under stirring of the obtained suspensions until complete water evaporation occurred, followed by drying at $90\text{ }^\circ\text{C}$ for 12 h and final calcination at $500\text{ }^\circ\text{C}$ for 2 h under air flow (heating ramp $5\text{ }^\circ\text{C}/\text{min}$).

3.2. Materials Characterization

The porosity of the materials was evaluated by the N_2 -adsorption isotherms at $-196\text{ }^\circ\text{C}$, using an ASAP 2010 (Micromeritics, Norcross, GA, USA) apparatus (from ReQuimTe Analyses Laboratory, Universidade Nova de Lisboa, Lisboa, Portugal). The samples were previously degassed at $300\text{ }^\circ\text{C}$ for 6 h. The specific surface area was calculated by the Brunauer–Emmett–Teller (BET) equation [75].

Structural characterization was carried out by means of X-ray diffraction (XRD) in a PAN'alytical X'Pert MPD equipped with a X'Celerator detector and secondary monochromator ($\text{Cu K}\alpha\ \lambda = 0.154\text{ nm}$, 50 kV, 40 mA; data recorded at a 0.017° step size, 100 s/step) in the University of Trás-os-Montes e Alto Douro. The collected spectra were analyzed by Rietveld refinement using PowderCell software, allowing the determination of crystallite sizes by means of the Williamson–Hall plot.

The redox properties were assessed by Temperature Programmed Reduction (TPR) experiments in an AMI-200 Catalyst Characterization Instrument (Altamira Instruments, Pittsburgh, PA, USA), employing H_2 as a reducing agent. In a typical H_2 -TPR experiment, 50 mg of the sample (grain size $180\text{--}355\ \mu\text{m}$) was heated up to $1100\text{ }^\circ\text{C}$ ($10\text{ }^\circ\text{C}/\text{min}$) under H_2 flow (1.5 cm^3) balanced with He (29 cm^3). The amount of H_2 consumed (mmol g^{-1}) was calculated by taking into account the integrated area of TPR peaks, calibrated against a known amount of CuO standard sample [76,77].

The surface composition and the chemical state of each element were determined by X-ray photoelectron spectroscopy (XPS) analyses, performed on a VG Scientific ESCALAB 200A spectrometer using Al $\text{K}\alpha$ radiation (1486.6 eV) in CEMUP. The charge effect was corrected using the $\text{C1s}'$ peak as a reference (binding energy of 285 eV). The CASAXPS software was used for data analysis.

The samples were imaged by transmission electron microscopy (TEM). The analyses were performed on a Leo 906E apparatus (Austin, TX, USA), at 120 kV in the University of Trás-os-Montes e Alto Douro. The samples were prepared by ultrasonic dispersion, and a 400 mesh formvar/carbon copper grid (Agar Scientific, Essex, UK) was dipped into the solution for the TEM analysis.

3.3. Catalytic Performance Evaluation

The catalytic studies for the N_2O decomposition took place in a quartz fixed-bed U-shaped reactor (0.8 cm i.d.) with 100 mg of catalyst loading (grain size $180\text{--}355\ \mu\text{m}$). The feed gas (1000 ppm N_2O and 0 or 2 vol. % O_2) total flow rate was $150\text{ cm}^3/\text{min}$ which corresponds to a Gas Hour Space Velocity (GHSV) of $40,000\text{ h}^{-1}$. The analysis of the gases was performed by a gas chromatograph (SHIMADZU 14B). The apparatus is equipped with a TCD detector and two separation columns (Molecular Sieve 5A for O_2 , N_2 measurements and Porapack QS for N_2O measurement). Prior to the catalytic activity measurements, the materials under consideration were subjected to further processing under He

flow ($100 \text{ cm}^3/\text{min}$) at $400 \text{ }^\circ\text{C}$. In order to minimize the external and internal diffusion limitations, preliminary experiments concerning the influence of particle size and W/F ratio on deN₂O catalytic performance were carried out. Based on these experiments, a catalyst particle size in the range of $180\text{--}355 \text{ }\mu\text{m}$ was selected, in addition to a W/F ratio of 0.04 g s cm^{-3} . The conversion of N₂O ($X_{\text{N}_2\text{O}}$) was calculated from the difference in N₂O concentration between the inlet and outlet gas streams, according to the equation

$$X_{\text{N}_2\text{O}}(\%) = \frac{[\text{N}_2\text{O}]_{\text{in}} - [\text{N}_2\text{O}]_{\text{out}}}{[\text{N}_2\text{O}]_{\text{in}}} \times 100 \quad (7)$$

The specific reaction rate (r , $\text{mol m}^{-2} \text{ s}^{-1}$) of the N₂O decomposition was also estimated using the following formula:

$$r \left(\text{mol m}^{-2} \text{ s}^{-1} \right) = \frac{X_{\text{N}_2\text{O}} \times [\text{N}_2\text{O}]_{\text{in}} \times F \left(\frac{\text{cm}^3}{\text{min}} \right)}{100 \times 60 \left(\frac{\text{s}}{\text{min}} \right) \times V_m \left(\frac{\text{cm}^3}{\text{mol}} \right) \times m_{\text{cat}} (\text{g}) \times S_{\text{BET}} \left(\frac{\text{m}^2}{\text{g}} \right)} \quad (8)$$

where F and V_m are the total flow rate and gas molar volume, respectively, at standard ambient temperature and pressure conditions (298 K and 1 bar), m_{cat} is the catalyst's mass and S_{BET} is the surface area.

4. Conclusions

In this work, three different ceria nanoshaped materials (nanorods, nanocubes and nanopolyhedra) were hydrothermally synthesized and used as supports for the cobalt oxide phase. Both single CeO₂ and Co/CeO₂ mixed oxides were catalytically assessed during the decomposition of N₂O in the presence and absence of oxygen. For bare ceria samples, the following deN₂O order was obtained: CeO₂-NR (nanorods) > CeO₂-NP (nanopolyhedra) > CeO₂-NC (nanocubes). Most importantly, cobalt addition to the CeO₂ carriers greatly enhances the N₂O decomposition, not affecting at all the order obtained for the bare ceria supports and clearly reflecting the key role of support. The present results clearly reveal the key role of support morphology on the textural, structural and redox properties, reflected then on the catalytic performance of Co₃O₄/CeO₂ mixed oxides. Among the different samples investigated, the cobalt-ceria nanorods (Co/CeO₂-NR) exposing {100} and {110} facets showed the best deN₂O performance, ascribed mainly to their abundance in Co²⁺ active sites in conjunction to their enhanced redox and textural properties.

Author Contributions: M.L. contributed to materials synthesis, results interpretation and paper writing; E.P. and N.K. contributed to catalytic evaluation studies; S.A.C.C. contributed to the materials characterization; M.K. contributed to the conception, design, results interpretation and writing of the paper; all authors contributed to the discussion and read and approved the final version of the manuscript.

Acknowledgments: The research work was supported by the Hellenic Foundation for Research and Innovation (HFRI) and the General Secretariat for Research and Technology (GSRT), under the HFRI PhD Fellowship grant (GA. no. 34252). This research has been cofinanced by the European Union and Greek national funds through the Operational Program Competitiveness, Entrepreneurship and Innovation, under the call RESEARCH—CREATE—INNOVATE (project code: T1EDK-00094). This work was also financially supported by Associate Laboratory LSRE-LCM—UID/EQU/50020/2019—funded by national funds through FCT/MCTES (PIDDAC). S.A.C.C. acknowledges Fundação para a Ciência e a Tecnologia (Portugal) for Investigador FCT program (IF/01381/2013/CP1160/CT0007), with financing from the European Social Fund and the Human Potential Operational Program. We are grateful to Carlos Sá (CEMUP) for the assistance with the XPS measurements, Pedro Tavares (UTAD) for the TEM and XRD analyses and Nuno Costa (ReQuimTe) for the N₂ adsorption results.

Conflicts of Interest: The authors declare no conflict of interest.

References

1. Konsolakis, M. Recent Advances on Nitrous Oxide (N₂O) Decomposition over Non-Noble-Metal Oxide Catalysts: Catalytic Performance, Mechanistic Considerations and Surface Chemistry Aspects. *ACS Catal.* **2015**, *5*, 6397–6421. [[CrossRef](#)]
2. Liu, Z.; He, F.; Ma, L.; Peng, S. Recent Advances in Catalytic Decomposition of N₂O on Noble Metal and Metal Oxide Catalysts. *Catal. Surv. Asia* **2016**, *20*, 121–132. [[CrossRef](#)]
3. Kim, M.J.; Lee, S.J.; Ryu, I.S.; Jeon, M.W.; Moon, S.H.; Roh, H.S.; Jeon, S.G. Catalytic decomposition of N₂O over cobalt based spinel oxides: The role of additives. *Mol. Catal.* **2017**, *442*, 202–207. [[CrossRef](#)]
4. Rutkowska, M. Catalytic Decomposition of N₂O Using a New Generation of Functionalized Microporous and Mesoporous Inorganic Materials. *Wiadomości Chemiczne* **2015**, *69*, 297–315.
5. Piumetti, M.; Hussain, M.; Fino, D.; Russo, N. Mesoporous silica supported Rh catalysts for high concentration N₂O decomposition. *Appl. Catal. B Environ.* **2015**, *165*, 158–168. [[CrossRef](#)]
6. Kim, S.S.; Lee, S.J.; Hong, S.C. Effect of CeO₂ addition to Rh/Al₂O₃ catalyst on N₂O decomposition. *Chem. Eng. J.* **2011**, *169*, 173–179. [[CrossRef](#)]
7. Hussain, M.; Fino, D.; Russo, N. Development of modified KIT-6 and SBA-15-spherical supported Rh catalysts for N₂O abatement: From powder to monolith supported catalysts. *Chem. Eng. J.* **2014**, *238*, 198–205. [[CrossRef](#)]
8. Wu, Y.; Cordier, C.; Berrier, E.; Nuns, N.; Dujardin, C.; Granger, P. Surface reconstructions of LaCo_{1-x}Fe_xO₃ at high temperature during N₂O decomposition in realistic exhaust gas composition: Impact on the catalytic properties. *Appl. Catal. B Environ.* **2013**, *140–141*, 151–163. [[CrossRef](#)]
9. Ivanov, D.V.; Pinaeva, L.G.; Isupova, L.A.; Sadovskaya, E.M.; Prosvirin, I.P.; Gerasimov, E.Y.; Yakovleva, I.S. Effect of surface decoration with LaSrFeO₄ on oxygen mobility and catalytic activity of La_{0.4}Sr_{0.6}FeO_{3-δ} in high-temperature N₂O decomposition, methane combustion and ammonia oxidation. *Appl. Catal. A Gen.* **2013**, *457*, 42–51. [[CrossRef](#)]
10. Kumar, S.; Vinu, A.; Subrt, J.; Bakardjieva, S.; Rayalu, S.; Teraoka, Y.; Labhsetwar, N. Catalytic N₂O decomposition on Pr_{0.8}Ba_{0.2}MnO₃ type perovskite catalyst for industrial emission control. *Catal. Today* **2012**, *198*, 125–132. [[CrossRef](#)]
11. Zhang, Y.; Wang, X.; Zhu, Y.; Zhang, T. Stabilization mechanism and crystallographic sites of Ru in Fe-promoted barium hexaaluminate under high-temperature condition for N₂O decomposition. *Appl. Catal. B Environ.* **2013**, *129*, 382–393. [[CrossRef](#)]
12. Zhang, Y.; Wang, X.; Zhu, Y.; Hou, B.; Yang, X.; Liu, X.; Wang, J.; Li, J.; Zhang, T. Characterization of Fe substitution into La-hexaaluminate systems and the effect on N₂O catalytic decomposition. *J. Phys. Chem. C* **2014**, *118*, 1999–2010. [[CrossRef](#)]
13. Zhang, Y.; Wang, X.; Zhu, Y.; Liu, X.; Zhang, T. Thermal evolution crystal structure and Fe crystallographic sites in LaFe_xAl_{12-x}O₁₉ hexaaluminates. *J. Phys. Chem. C* **2014**, *118*, 10792–10804. [[CrossRef](#)]
14. Pérez-Ramírez, J.; Santiago, M. Metal-substituted hexaaluminates for high-temperature N₂O abatement. *Chem. Commun.* **2007**, *2*, 619–621. [[CrossRef](#)] [[PubMed](#)]
15. Stelmachowski, P.; Maniak, G.; Kaczmarczyk, J.; Zasada, F.; Piskorz, W.; Kotarba, A.; Sojka, Z. Mg and Al substituted cobalt spinels as catalysts for low temperature deN₂O-Evidence for octahedral cobalt active sites. *Appl. Catal. B Environ.* **2014**, *146*, 105–111. [[CrossRef](#)]
16. Grzybek, G.; Stelmachowski, P.; Gudyka, S.; Duch, J.; Ćmil, K.; Kotarba, A.; Sojka, Z. Insights into the twofold role of Cs doping on deN₂O activity of cobalt spinel catalyst-towards rational optimization of the precursor and loading. *Appl. Catal. B Environ.* **2015**, *168–169*, 509–514. [[CrossRef](#)]
17. Zasada, F.; Piskorz, W.; Janas, J.; Gryboś, J.; Indyka, P.; Sojka, Z. Reactive Oxygen Species on the (100) Facet of Cobalt Spinel Nanocatalyst and their Relevance in ¹⁶O₂/¹⁸O₂ Isotopic Exchange, deN₂O, and deCH₄ Processes-A Theoretical and Experimental Account. *ACS Catal.* **2015**, *5*, 6879–6892. [[CrossRef](#)]
18. Amrousse, R.; Chang, P.-J.; Choklati, A.; Friche, A.; Rai, M.; Bachar, A.; Follet-Houttemane, C.; Hori, K. Catalytic decomposition of N₂O over Ni and Mg-magnetite catalysts. *Catal. Sci. Technol.* **2013**, *3*, 2288. [[CrossRef](#)]
19. Zou, W.; Xie, P.; Hua, W.; Wang, Y.; Kong, D.; Yue, Y.; Ma, Z.; Yang, W.; Gao, Z. Catalytic decomposition of N₂O over Cu-ZSM-5 nanosheets. *J. Mol. Catal. A Chem.* **2014**, *394*, 83–88. [[CrossRef](#)]

20. Zhang, X.; Shen, Q.; He, C.; Ma, C.; Cheng, J.; Liu, Z.; Hao, Z. Decomposition of nitrous oxide over Co-zeolite catalysts: role of zeolite structure and active site. *Catal. Sci. Technol.* **2012**, *2*, 1249–1258. [[CrossRef](#)]
21. Rutkowska, M.; Piwowarska, Z.; Micek, E.; Chmielarz, L. Hierarchical Fe-, Cu- and Co-Beta zeolites obtained by mesotemplate-free method. Part I: Synthesis and catalytic activity in N₂O decomposition. *Microporous Mesoporous Mater.* **2015**, *209*, 54–65. [[CrossRef](#)]
22. Xie, P.; Luo, Y.; Ma, Z.; Wang, L.; Huang, C.; Yue, Y.; Hua, W.; Gao, Z. CoZSM-11 catalysts for N₂O decomposition: Effect of preparation methods and nature of active sites. *Appl. Catal. B Environ.* **2015**, *170–171*, 34–42. [[CrossRef](#)]
23. Grzybek, G.; Stelmachowski, P.; Gudyka, S.; Indyka, P.; Sojka, Z.; Guillén-Hurtado, N.; Rico-Pérez, V.; Bueno-López, A.; Kotarba, A. Strong dispersion effect of cobalt spinel active phase spread over ceria for catalytic N₂O decomposition: The role of the interface periphery. *Appl. Catal. B Environ.* **2016**, *180*, 622–629. [[CrossRef](#)]
24. Chromčáková, Ž.; Obalová, L.; Kovanda, F.; Legut, D.; Titov, A.; Ritz, M.; Fridrichová, D.; Michalik, S.; Kušrowski, P.; Jiráková, K. Effect of precursor synthesis on catalytic activity of Co₃O₄ in N₂O decomposition. *Catal. Today* **2015**, *257*, 18–25. [[CrossRef](#)]
25. Franken, T.; Palkovits, R. Investigation of potassium doped mixed spinels Cu_xCo_{3-x}O₄ as catalysts for an efficient N₂O decomposition in real reaction conditions. *Appl. Catal. B Environ.* **2015**, *176–177*, 298–305. [[CrossRef](#)]
26. Zabitskiy, M.; Erjavec, B.; Djinović, P.; Pintar, A. Ordered mesoporous CuO-CeO₂ mixed oxides as an effective catalyst for N₂O decomposition. *Chem. Eng. J.* **2014**, *254*, 153–162. [[CrossRef](#)]
27. Xue, L.; He, H.; Liu, C.; Zhang, C.; Zhang, B. Promotion Effects and Mechanism of Alkali Metals and Alkaline Earth Metals on Cobalt - Cerium Composite Oxide Catalysts for N₂O Decomposition. *Environ. Sci. Technol.* **2009**, *43*, 890–895. [[CrossRef](#)] [[PubMed](#)]
28. Liu, Z.; He, C.; Chen, B.; Liu, H. CuO-CeO₂ mixed oxide catalyst for the catalytic decomposition of N₂O in the presence of oxygen. *Catal. Today* **2017**, *297*, 78–83. [[CrossRef](#)]
29. Russo, N.; Fino, D.; Saracco, G.; Specchia, V. N₂O catalytic decomposition over various spinel-type oxides. *Catal. Today* **2007**, *119*, 228–232. [[CrossRef](#)]
30. Xue, L.; Zhang, C.; He, H.; Teraoka, Y. Catalytic decomposition of N₂O over CeO₂ promoted Co₃O₄ spinel catalyst. *Appl. Catal. B Environ.* **2007**, *75*, 167–174. [[CrossRef](#)]
31. Yang, J.; Lukashuk, L.; Akbarzadeh, J.; Stöger-Pollach, M.; Peterlik, H.; Föttinger, K.; Rupprechter, G.; Schubert, U. Different Synthesis Protocols for Co₃O₄-CeO₂ Catalysts-Part 1: Influence on the Morphology on the Nanoscale. *Chem. Eur. J.* **2015**, *21*, 885–892. [[CrossRef](#)] [[PubMed](#)]
32. Shen, Q.; Li, L.; Li, J.; Tian, H.; Hao, Z. A study on N₂O catalytic decomposition over Co/MgO catalysts. *J. Hazard. Mater.* **2009**, *163*, 1332–1337. [[CrossRef](#)] [[PubMed](#)]
33. Luo, J.-Y.; Meng, M.; Li, X.; Li, X.-G.; Zha, Y.-Q.; Hu, T.-D.; Xie, Y.-N.; Zhang, J. Mesoporous Co₃O₄-CeO₂ and Pd/Co₃O₄-CeO₂ catalysts: Synthesis, characterization and mechanistic study of their catalytic properties for low-temperature CO oxidation. *J. Catal.* **2008**, *254*, 310–324. [[CrossRef](#)]
34. Wang, H.; Ye, J.L.; Liu, Y.; Li, Y.D.; Qin, Y.N. Steam reforming of ethanol over Co₃O₄/CeO₂ catalysts prepared by different methods. *Catal. Today* **2007**, *129*, 305–312. [[CrossRef](#)]
35. Qiu, N.; Zhang, J.; Wu, Z. Peculiar surface-interface properties of nanocrystalline ceria-cobalt oxides with enhanced oxygen storage capacity. *Phys. Chem. Chem. Phys.* **2014**, *16*, 22659–22664. [[CrossRef](#)] [[PubMed](#)]
36. Vinod, C.P. Surface science as a tool for probing nanocatalysis phenomena. *Catal. Today* **2010**, *154*, 113–117. [[CrossRef](#)]
37. Hu, P.; Huang, Z.; Amghouz, Z.; Makkee, M.; Xu, F.; Kapteijn, F.; Dikhtiarenko, A.; Chen, Y.; Gu, X.; Tang, X. Electronic Metal-Support Interactions in Single-Atom Catalysts. *Angew. Chem.* **2014**, *126*, 3486–3489. [[CrossRef](#)]
38. Elias, J.S.; Risch, M.; Giordano, L.; Mansour, A.N.; Shao-Horn, Y. Structure, Bonding, and Catalytic Activity of Monodisperse, Transition-Metal-Substituted CeO₂ Nanoparticles. *J. Am. Chem. Soc.* **2014**, *136*, 17193–17200. [[CrossRef](#)] [[PubMed](#)]
39. Cargnello, M.; Fornasiero, P.; Gorte, R.J. Opportunities for tailoring catalytic properties through metal-support interactions. *Catal. Lett.* **2012**, *142*, 1043–1048. [[CrossRef](#)]
40. Díez-Ramírez, J.; Sánchez, P.; Kyriakou, V.; Zafeiratos, S.; Marnellos, G.E.; Konsolakis, M.; Dorado, F. Effect of support nature on the cobalt-catalyzed CO₂ hydrogenation. *J. CO₂ Util.* **2017**, *21*, 562–571. [[CrossRef](#)]

41. Cargnello, M.; Doan-Nguyen, V.V.T.; Gordon, T.R.; Diaz, R.E.; Stach, E.A.; Gorte, R.J.; Fornasiero, P.; Murray, C.B. Control of Metal Nanocrystal Size Reveals Metal-Support Interface Role for Ceria Catalysts. *Science* **2013**, *341*, 771–773. [[CrossRef](#)] [[PubMed](#)]
42. Vayssilov, G.N.; Lykhach, Y.; Migani, A.; Staudt, T.; Petrova, G.P.; Tsud, N.; Skála, T.; Bruix, A.; Illas, F.; Prince, K.C.; et al. Support nanostructure boosts oxygen transfer to catalytically active platinum nanoparticles. *Nat. Mater.* **2011**, *10*, 310–315. [[CrossRef](#)] [[PubMed](#)]
43. Mahammadunnisa, S.K.; Akanksha, T.; Krushnamurty, K.; Subrahmanyam, C. Catalytic decomposition of N₂O over CeO₂ supported Co₃O₄ catalysts. *J. Chem. Sci.* **2016**, *128*, 1795–1804. [[CrossRef](#)]
44. Lin, B.; Liu, Y.; Heng, L.; Ni, J.; Lin, J.; Jiang, L. Effect of ceria morphology on the catalytic activity of Co/CeO₂ catalyst for ammonia synthesis. *Catal. Commun.* **2017**, *101*, 15–19. [[CrossRef](#)]
45. Zabilskiy, M.; Djinić, P.; Tchernychova, E.; Tkachenko, O.P.; Kustov, L.M.; Pintar, A. Nanoshaped CuO/CeO₂ Materials: Effect of the Exposed Ceria Surfaces on Catalytic Activity in N₂O Decomposition Reaction. *ACS Catal.* **2015**, *5*, 5357–5365. [[CrossRef](#)]
46. Andrade-Martínez, J.; Ortega-Zarzosa, G.; Gómez-Cortés, A.; Rodríguez-González, V. N₂O catalytic reduction over different porous SiO₂ materials functionalized with copper. *Powder Technol.* **2015**, *274*, 305–312. [[CrossRef](#)]
47. Mei, J.; Ke, Y.; Yu, Z.; Hu, X.; Qu, Z.; Yan, N. Morphology-dependent properties of Co₃O₄/CeO₂ catalysts for low temperature dibromomethane (CH₂Br₂) oxidation. *Chem. Eng. J.* **2017**, *320*, 124–134. [[CrossRef](#)]
48. Hu, F.; Peng, Y.; Chen, J.; Liu, S.; Song, H.; Li, J. Low content of CoO_x supported on nanocrystalline CeO₂ for toluene combustion: The importance of interfaces between active sites and supports. *Appl. Catal. B Environ.* **2019**, *240*, 329–336. [[CrossRef](#)]
49. Lykaki, M.; Pachatouridou, E.; Carabineiro, S.A.C.; Iliopoulou, E.; Andriopoulou, C.; Kallithrakas-Kontos, N.; Boghosian, S.; Konsolakis, M. Ceria nanoparticles shape effects on the structural defects and surface chemistry: Implications in CO oxidation by Cu/CeO₂ catalysts. *Appl. Catal. B Environ.* **2018**, *230*, 18–28. [[CrossRef](#)]
50. Allwar, A.; Md Noor, A.; Nawi, M. Textural Characteristics of Activated Carbons Prepared from Oil Palm Shells Activated with ZnCl₂ and Pyrolysis Under Nitrogen and Carbon Dioxide. *J. Phys. Sci.* **2008**, *19*, 93–104.
51. Kumar, S.; Sharma, C. Synthesis, characterization and catalytic wet air oxidation property of mesoporous Ce_{1-x}Fe_xO₂ mixed oxides. *Mater. Chem. Phys.* **2015**, *155*, 223–231.
52. Tan, L.; Tao, Q.; Gao, H.; Li, J.; Jia, D.; Yang, M. Preparation and catalytic performance of mesoporous ceria-base composites CuO/CeO₂, Fe₂O₃/CeO₂ and La₂O₃/CeO₂. *J. Porous Mater.* **2017**, *24*, 795–803. [[CrossRef](#)]
53. Farahmandjou, M.; Zarinkamar, M. Synthesis of nano-sized ceria (CeO₂) particles via a cerium hydroxy carbonate precursor and the effect of reaction temperature on particle morphology. *J. Ultrafine Grained Nanostructured Mater.* **2015**, *48*, 5–10.
54. Sharma, V.; Eberhardt, K.M.; Sharma, R.; Adams, J.B.; Crozier, P.A. A spray drying system for synthesis of rare-earth doped cerium oxide nanoparticles. *Chem. Phys. Lett.* **2010**, *495*, 280–286. [[CrossRef](#)]
55. Liu, J.; Zhao, Z.; Wang, J.; Xu, C.; Duan, A.; Jiang, G.; Yang, Q. The highly active catalysts of nanometric CeO₂-supported cobalt oxides for soot combustion. *Appl. Catal. B Environ.* **2008**, *84*, 185–195. [[CrossRef](#)]
56. Yu, S.W.; Huang, H.H.; Tang, C.W.; Wang, C.B. The effect of accessible oxygen over Co₃O₄-CeO₂ catalysts on the steam reforming of ethanol. *Int. J. Hydrogen Energy* **2014**, *39*, 20700–20711. [[CrossRef](#)]
57. Konsolakis, M.; Carabineiro, S.A.C.; Marnellos, G.E.; Asad, M.F.; Soares, O.S.G.P.; Pereira, M.F.R.; Órfão, J.J.M.; Figueiredo, J.L. Effect of cobalt loading on the solid state properties and ethyl acetate oxidation performance of cobalt-cerium mixed oxides. *J. Colloid Interface Sci.* **2017**, *496*, 141–149. [[CrossRef](#)] [[PubMed](#)]
58. Mock, S.A.; Sharp, S.E.; Stoner, T.R.; Radetic, M.J.; Zell, E.T.; Wang, R. CeO₂ nanorods-supported transition metal catalysts for CO oxidation. *J. Colloid Interface Sci.* **2016**, *466*, 261–267. [[CrossRef](#)] [[PubMed](#)]
59. Wang, Y.; Hu, X.; Zheng, K.; Zhang, H.; Zhao, Y. Effect of precipitants on the catalytic activity of Co–Ce composite oxide for N₂O catalytic decomposition. *Reac. Kinet. Mech. Cat.* **2018**, *123*, 707–721. [[CrossRef](#)]
60. Wang, L.; Liu, H. Mesoporous Co–CeO₂ catalyst prepared by colloidal solution combustion method for reverse water-gas shift reaction. *Catal. Today* **2018**, *316*, 155–161. [[CrossRef](#)]

61. Kumar Megarajan, S.; Rayalu, S.; Teraoka, Y.; Labhsetwar, N. High NO oxidation catalytic activity on non-noble metal based cobalt-ceria catalyst for diesel soot oxidation. *J. Mol. Catal. A Chem.* **2014**, *385*, 112–118. [[CrossRef](#)]
62. Konsolakis, M. The role of Copper–Ceria interactions in catalysis science: Recent theoretical and experimental advances. *Appl. Catal. B Environ.* **2016**, *198*, 49–66. [[CrossRef](#)]
63. Cui, Y.; Dai, W.-L. Support morphology and crystal plane effect of Cu/CeO₂ nanomaterial on the physicochemical and catalytic properties for carbonate hydrogenation. *Catal. Sci. Technol.* **2016**, *6*, 7752–7762. [[CrossRef](#)]
64. Guo, X.; Zhou, R. A new insight into the morphology effect of ceria on CuO/CeO₂ catalysts for CO selective oxidation in hydrogen-rich gas. *Catal. Sci. Technol.* **2016**, *6*, 3862–3871. [[CrossRef](#)]
65. Wang, C.; Cheng, Q.; Wang, X.; Ma, K.; Bai, X.; Tan, S.; Tian, Y.; Ding, T.; Zheng, L.; Zhang, J.; et al. Enhanced catalytic performance for CO preferential oxidation over CuO catalysts supported on highly defective CeO₂ nanocrystals. *Appl. Surf. Sci.* **2017**, *422*, 932–943. [[CrossRef](#)]
66. Dou, J.; Tang, Y.; Nie, L.; Andolina, C.M.; Zhang, X.; House, S.; Li, Y.; Yang, J.; Tao, F.F. Complete Oxidation of Methane on Co₃O₄/CeO₂ Nanocomposite: A Synergic Effect. *Catal. Today* **2018**, *311*, 48–55. [[CrossRef](#)]
67. Konsolakis, M.; Sgourakis, M.; Carabineiro, S.A.C. Surface and redox properties of cobalt-ceria binary oxides: On the effect of Co content and pretreatment conditions. *Appl. Surf. Sci.* **2015**, *341*, 48–54. [[CrossRef](#)]
68. Ma, J.; Rodriguez, N.M.; Vannice, M.A.; Baker, R.T.K. Nitrous oxide decomposition and reduction over copper catalysts supported on various types of carbonaceous materials. *Top. Catal.* **2000**, *10*, 27–38. [[CrossRef](#)]
69. You, Y.; Chang, H.; Ma, L.; Guo, L.; Qin, X.; Li, J.; Li, J. Enhancement of N₂O decomposition performance by N₂O pretreatment over Ce-Co-O catalyst. *Chem. Eng. J.* **2018**, *347*, 184–192. [[CrossRef](#)]
70. Iwanek, E.; Krawczyk, K.; Petryk, J.; Sobczak, J.W.; Kaszkur, Z. Direct nitrous oxide decomposition with CoO_x-CeO₂ catalysts. *Appl. Catal. B Environ.* **2011**, *106*, 416–422. [[CrossRef](#)]
71. Piskorz, W.; Zasada, F.; Stelmachowski, P.; Kotarba, A.; Sojka, Z. Decomposition of N₂O over the surface of cobalt spinel: A DFT account of reactivity experiments. *Catal. Today* **2008**, *137*, 418–422. [[CrossRef](#)]
72. Abu-Zied, B.M.; Soliman, S.A.; Abdellah, S.E. Pure and Ni-substituted Co₃O₄ spinel catalysts for direct N₂O decomposition. *Chin. J. Catal.* **2014**, *35*, 1105–1112. [[CrossRef](#)]
73. Stelmachowski, P.; Maniak, G.; Kotarba, A.; Sojka, Z. Strong electronic promotion of Co₃O₄ towards N₂O decomposition by surface alkali dopants. *Catal. Commun.* **2009**, *10*, 1062–1065. [[CrossRef](#)]
74. Savereide, L.; Nauert, S.L.; Roberts, C.A.; Notestein, J.M. The effect of support morphology on CoO_x/CeO₂ catalysts for the reduction of NO by CO. *J. Catal.* **2018**, *366*, 150–158. [[CrossRef](#)]
75. Brunauer, S.; Emmett, P.H.; Teller, E. Adsorption of Gases in Multimolecular Layers. *J. Am. Chem. Soc.* **1938**, *60*, 309–319. [[CrossRef](#)]
76. Barthos, R.; Hegyessy, A.; Klébert, S.; Valyon, J. Vanadium dispersion and catalytic activity of Pd/VO_x/SBA-15 catalysts in the Wacker oxidation of ethylene. *Microporous Mesoporous Mater.* **2015**, *207*, 1–8. [[CrossRef](#)]
77. Xu, J.; Harmer, J.; Li, G.; Chapman, T.; Collier, P.; Longworth, S.; Tsang, S.C. Size dependent oxygen buffering capacity of ceria nanocrystals. *Chem. Commun.* **2010**, *46*, 1887–1889. [[CrossRef](#)] [[PubMed](#)]

